scientific reports

Check for updates

OPEN

Novel two dimensional B2C3 monolayer as a high theoretical capacity anode material for Li or Na ion batteries

Xi Zhu[1,5], Keyang Wu[2,5], Beibei Ma[3], Xiao Wang[4], Detong Kong[2]✉ & Yuan Wang[2]✉

In this study, we utilized first-principles calculations to design a novel class of two-dimensional (2D) polycyclic materials composed of carbon and boron atoms, termed *k*-B_2C_3, which hold significant promise as high-capacity, fast-diffusing anode materials for Li/Na-ion batteries. We investigated the thermodynamic stability, mechanical properties, electronic structure, and energy storage characteristics of *k*-B_2C_3. The results reveal that *k*-B_2C_3 exhibits a density of states at the Fermi level of 0.18 states/eV, a Young's modulus of $274.43\mathrm{GPa}\cdot\mathrm{mm}$, and a Poisson's ratio of 0.43, indicating excellent metallic conductivity and mechanical ductility, which are crucial for stability during charge/discharge cycles. Furthermore, the Li/Na diffusion barriers for *k*-B_2C_3 are 0.55 eV and 0.17 eV, respectively, which are vital for efficient charge/discharge processes. Most notably, *k*-B_2C_3 demonstrates a high theoretical storage capacity of 930 $mAhg^{-1}$ for both Li and Na, coupled with low open-circuit voltages (1.30–0.54 V for Li and 1.17–0.34 V for Na). These findings suggest that 2D *k*-B_2C_3 is a promising candidate for use as an anode material in Li/Na-ion batteries and provides valuable insights for the development of advanced 2D electrode materials.

With the rise of the global electric vehicle industry, lithium-ion batteries (LIBs) have gained widespread adoption due to their high reliability, long cycle life, and other advantages[1]. However, current lithium-ion batteries face several challenges, including limited capacity, low cost-effectiveness, safety concerns, insufficient global lithium resources, and significant price fluctuations, which hinder their ability to fully meet the growing demand for energy storage[2–6]. Consequently, the search for more economical, safer, and sustainable alternatives has become a key direction in battery development. In contrast to lithium, sodium is more abundant, offers higher safety, superior energy density, and excellent high-temperature performance, making Sodium-ion batteries (NIBs) one of the most promising alternatives to LIBs[7,8]. Developing high-performance advanced electrode materials has thus become a major research focus in this field[9].

In recent years, significant efforts have been dedicated to the development of electrode materials suitable for LIBs/NIBs[10–13]. Among these materials, two-dimensional (2D) materials have garnered considerable attention due to their high surface area and unique physicochemical properties, such as graphene, carbides, and phosphides[14–16]. However, most of the 2D anode materials studied to date have failed to address critical issues, such as the structural stability of the material and the formation of Li/Na dendrites during the energy storage process, which in turn leads to a significant reduction in energy storage capacity. Therefore, the development of high-performance 2D anode materials for NIBs, with excellent energy storage capability, electrochemical performance, mechanical properties, and thermal stability, remains a major challenge[17–20].

Previous studies have shown that doping 2D materials with elements such as P, B, and Ta can enhance their energy storage performance[21–23]. In this context, we propose a novel 2D material, termed *k*-B_2C_3, and predict its structural properties through first-principles calculations. The results indicate that *k*-B_2C_3 possesses stable mechanical properties and thermal stability, exhibits high electrical conductivity, and demonstrates excellent energy storage capability. Both sodium and lithium atoms experience low diffusion barriers and high specific capacities within this material. Therefore, the 2D material based on *k*-B_2C_3 holds great potential as a high-

[1]Chongqing Electromechanical Holdings (Group) Co., Ltd, Chongqing 401123, China. [2]School of Machinery and Communications, Southwest Forestry University, Kunming 650224, China. [3]CNOOC Fujian Natural Gas Co., Ltd, Fujian 350001, China. [4]City College, Kunming University of Science and Technology, Kunming 650093, China. [5]Xi Zhu and Keyang Wu contributed equally to this work and should be considered co-first authors. ✉email: 228276045@qq.com; wyuan88@126.com

performance electrode material. We believe that k-B_2C_3 based 2D materials can serve as an excellent candidate for high-performance anode materials in batteries.

Computational details

The first-principles calculations were performed using the Vienna Ab Initio Simulation Package (VASP)[24], based on density functional theory (DFT). The interaction between valence and core electrons was treated using the projector augmented wave (PAW) method, and the exchange–correlation energy was approximated using the Perdew-Burke-Ernzerhof (PBE) generalized gradient approximation (GGA)[25,26]. To minimize interactions between adjacent layers, a 20 Å vacuum layer was introduced along the perpendicular direction. To ensure the reliability of the calculated values, we performed a k-point convergence test. Figure S1 shows that the total energy converges with increasing k-point sampling density. Therefore, we employed a $5\times5\times1$ Monkhorst–Pack grid[27] and a plane-wave basis set with a cutoff energy of 500 eV to ensure the self-consistent convergence of the total energy and atomic forces. The convergence criteria for total energy and forces were set to 10^{-6} eV and 0.01 eV·Å^{-1}, respectively. The diffusion barriers for Li/Na ions were calculated using the climbing-image nudged elastic band (CI-NEB) method[28], employing a $3\times2\times1$ supercell. The phonon dispersion was calculated using the PHONOPY code[29]. To assess the thermal stability of k-B_2C_3, ab initio molecular dynamics (AIMD) simulations[30] were performed at 300 K under standard NVT conditions. For energy storage calculations in adsorption structures, Li/Na atoms were randomly distributed on both sides of the k-B_2C_3 monolayer at different atomic concentrations to determine the maximum storage capacity, M_n k-B_2C_3 (M = Li, Na)[22]. Additionally, the electronic band structure was precisely calculated using the Heyd–Scuseria–Ernzerhof (HSE06) functional[31].

Results and discussion

Structural stability and electronic properties of k-C_2B_3

As shown in Fig. 1, the crystal structure of k-B_2C_3 is a two-dimensional configuration composed of hexagonal and octagonal rings formed by carbon (C) and boron (B) atoms, with adjacent octagonal chains covalently bonded by C = C bonds. In the figure, blue represents C atoms and brown represents B atoms. The unit cell of k-B_2C_3 belongs to the space group with PMMM symmetry. After full structural optimization, the lattice constants were obtained as a = 2.73 Å, b = 5.87 Å, with three distinct bond lengths. The longest B-B bond is 1.692 Å, followed by the C-B bond at 1.566 Å, and the shortest C = C bond at 1.322 Å, corresponding to the bonds labeled l_1–l_3 in Fig. 1. Moreover, the bond angles within the hexagonal and octagonal rings in k-B_2C_3 are 121.4° and 119.3°, respectively, indicating that k-B_2C_3 possesses unique electronic properties and adsorption activity.

To investigate the dynamic and thermodynamic stability as well as the conductivity of k-B_2C_3, we performed calculations on its phonon spectrum, AIMD simulations, total energy, and electronic band structure. As shown in Fig. 2a, the phonon band structure of k-B_2C_3 does not exhibit any imaginary frequencies throughout the entire Brillouin zone, indicating that k-B_2C_3 is a dynamically stable structure. To further examine the thermal stability of k-B_2C_3, AIMD simulations were conducted using a $3\times2\times1$ supercell at 300 K for 3 ps, with a time step of 1 fs[32]. The results, shown in Fig. 2b, reveal that the average potential energy remains constant throughout the heating process, and no structural reconstruction was observed, indicating that k-B_2C_3 maintains thermal stability at least up to 300 K.

In Fig. 2c, the total energy of k-B_2C_3 was compared with that of graphyne, Bi_2Te_2Se, Bi_2Te_2S, kust-α, and penta-graphene[33–35]. The results indicate that k-B_2C_3 is more stable than all materials except for kust-α. To further confirm the conductivity of k-B_2C_3 as a potential electrode material, we analyzed its electronic band structure and density of states. As shown in Fig. 2d, both PBE and HSE06 calculations reveal no band gap, with the occupied states crossing the Fermi level, indicating its metallic behavior. Moreover, k-B_2C_3 exhibits a density of states at the Fermi level of 0.18 states/eV, further supporting its excellent electrical conductivity, which is crucial for efficient charge transport in electrode applications.

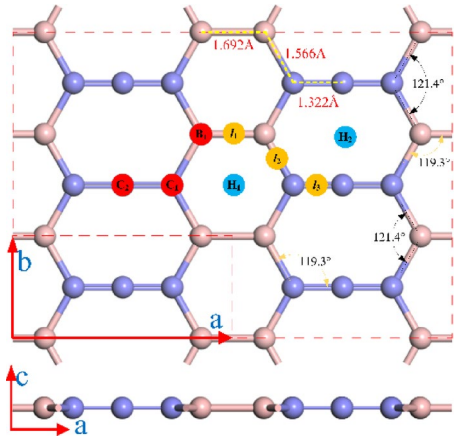

Fig. 1. Crystal structure of the k-B_2C_3.

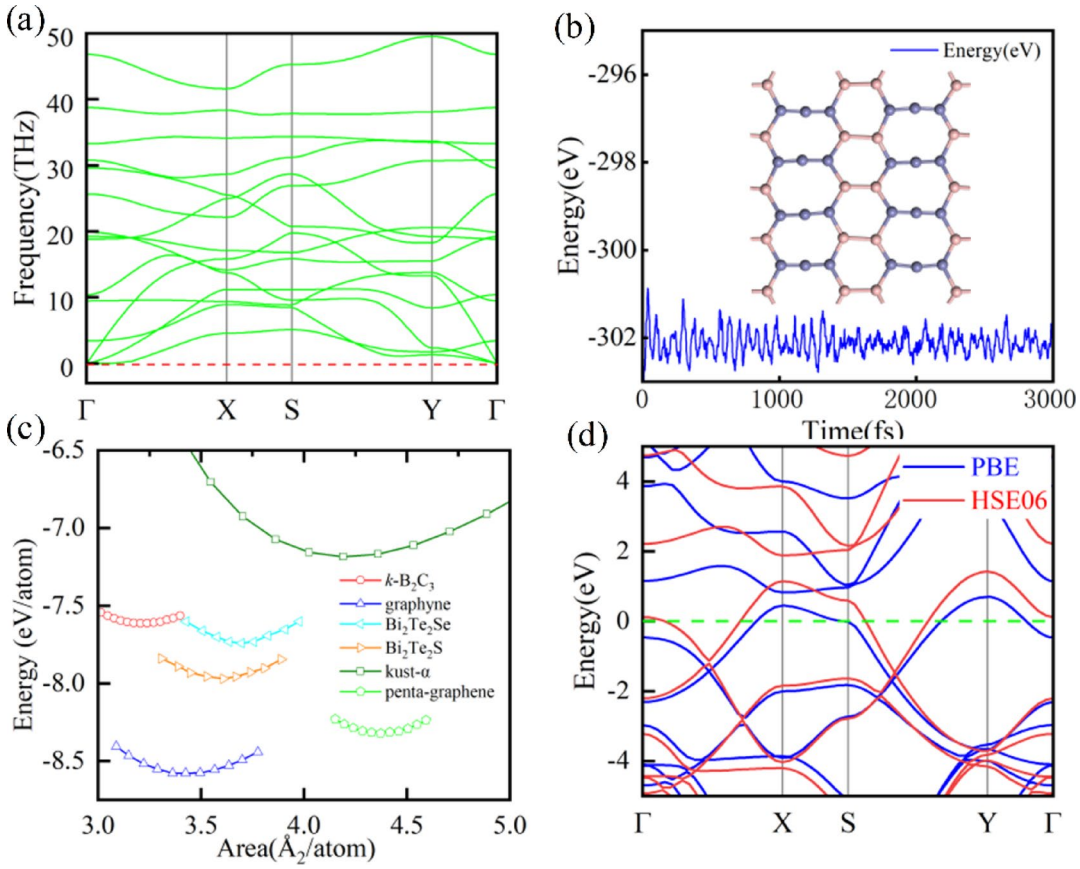

Fig. 2. (**a**) Phonon band structure of *k*-B_2C_3, showing no imaginary frequencies, indicating dynamic stability. (**b**) Potential energy fluctuations of *k*-B_2C_3 during AIMD simulations at 300 K, confirming thermal stability. (**c**) Total energy comparison of *k*-B_2C_3 with other 2D materials[33–35], showing its relative stability. (**d**) Electronic band structure of *k*-B_2C_3, calculated with PBE and HSE06, revealing metallic behavior with no band gap.

In the lattice system of *k*-B_2C_3, there are four independent elastic constants, and the strain energy and elastic constants can be calculated using the following Eq. (1):[36]

$$E_{strain} = \frac{1}{2}\left(C_{11}\varepsilon_a^2 + C_{22}\varepsilon_b^2\right) + C_{12}\varepsilon_a\varepsilon_b + 2C_{44}\varepsilon_{ab}^2 \tag{1}$$

Here, E_{strain} represents the strain energy per unit area, C_{11}, C_{12}, C_{22}, and C_{44} are the four independent elastic constants, and ε_a, ε_a, and ε_{ab} represent the strains along the *a*, *b*, and shear directions, respectively. By fitting the curves related to uniaxial, biaxial, and shear strains, the following elastic constants were obtained: $C_{11} = 239.07GPa \cdot mm$, $C_{12} = 34.86GPa \cdot mm$, $C_{22} = 217.51GPa \cdot mm$, and $C_{44} = 94.61GPa \cdot mm$. Since $C_{11}C_{22} - C_{12}^2 > 0$, $C_{44} > 0$, the Born-Huang criterion is satisfied, indicating that the mechanical structure of *k*-B_2C_3 is stable.

To further assess whether the material may undergo volumetric deformation during the charge–discharge process, we calculated the Young's modulus (*C*) and Poisson's ratio (*v*) of *k*-B_2C_3, which were obtained from Eqs. (2) and (3), respectively.

$$C(\theta) = \frac{C_{11}C_{22} - C_{12}^2}{C_{11}a^4 + C_{22}\beta^4 + \left(\frac{C_{11}C_{22}-C_{12}^2}{C_{44}} - 2C_{12}\right)\alpha^4\beta^4} \tag{2}$$

$$v(\theta) = \frac{\left(C_{11} + C_{22} - \frac{C_{11}C_{22}-C_{12}^2}{C_{44}}\right)\alpha^2\beta^2 - C_{12}\left(\alpha^4 + \beta^4\right)}{C_{11}\alpha^4 + C_{22}\beta^4 + \left(\frac{C_{11}C_{22}-C_{12}^2}{C_{44}} - 2C_{12}\right)\alpha^2\beta^2} \tag{3}$$

In the equation, $\alpha = \cos\theta$ and $\beta = \sin\theta$, where θ is the angle along the a-direction. $C(\theta)$ and $v(\theta)$ represent the Young's modulus and Poisson's ratio, respectively, for the plane at angle θ. As shown in Fig. 3a, b, the Young's modulus and Poisson's ratio of *k*-B_2C_3 are presented in polar coordinates. From Fig. 3a, it can be seen that the material exhibits orthogonal symmetry, indicating anisotropic mechanical properties. The Young's moduli of

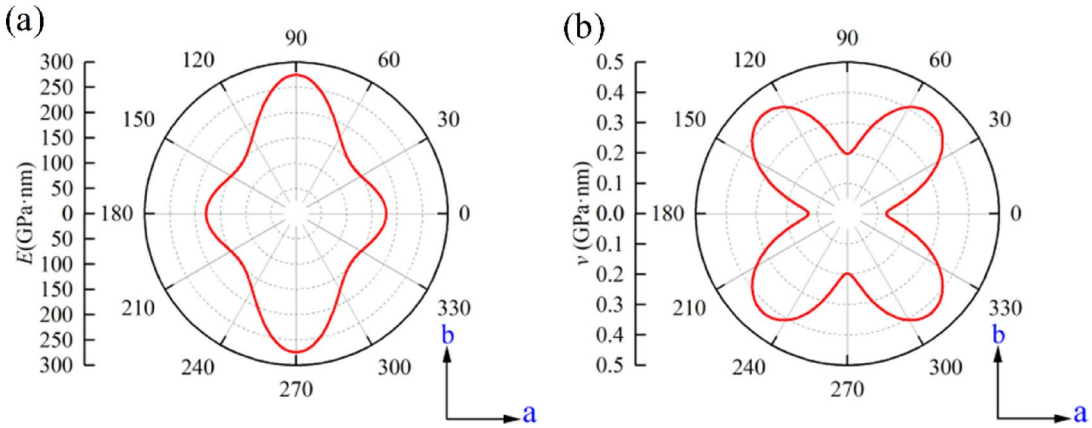

Fig. 3. Mechanical properties of k-B_2C_3. (**a**) Polar diagram for in-plane Young's modulus. (**b**) Polar diagram for Poisson's ratio.

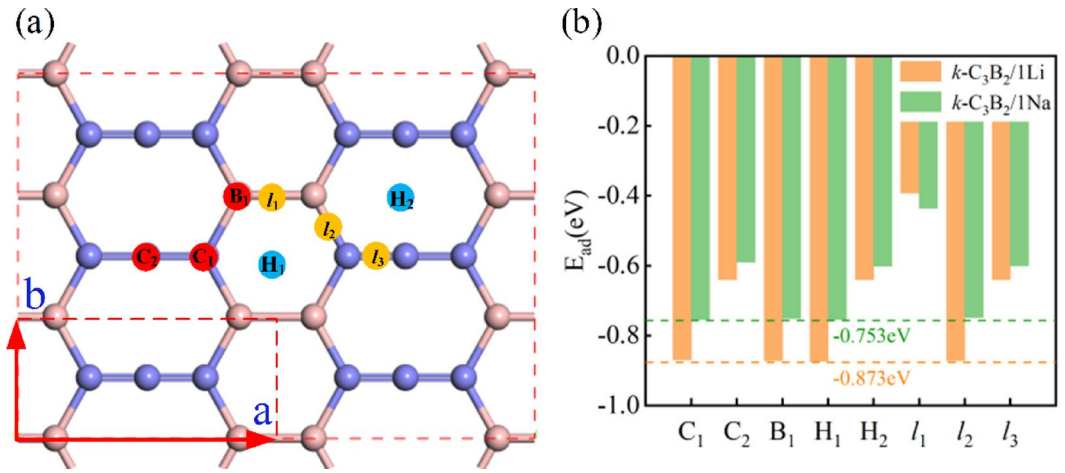

Fig. 4. (**a**) The inequivalent adsorption sites in k-B_2C_3, labeled as C, B, H, and l. (**b**) Adsorption energies of a single Li/Na atom at the sites l_1,l_2, l_3,H_1, H_2,C_1, C_2, and B_1 on the k-B_2C_3 structure.

k-B_2C_3 along the a-axis and b-axis are 145.17 GPa·mm and 274.43 GPa·mm, respectively, both lower than that of graphene, suggesting that k-B_2C_3 is softer than graphene. The Poisson's ratios of k-B_2C_3 along the a-axis and b-axis are 0.1 and 0.4, respectively. Combined with the Young's modulus, this indicates that the material is more ductile along the a-direction and more resistant to deformation along the b-direction[37]. Therefore, k-B_2C_3 can effectively prevent deformation during charge–discharge cycles, making it more suitable for use as an electrode material in batteries.

Adsorption and diffusion of single Li/Na atom on k-B_2C_3

To more accurately determine the optimal adsorption sites in the k-B_2C_3 structure, we calculated the adsorption energies at eight possible adsorption points (C_1, C_2, B_1, H_1, H_2, L_1, L_2, L_3) shown in Fig. 4a. Specifically, C_1 and C_2 correspond to the top sites of different C atoms, B_1 corresponds to the top site of a B atom, L_1, L_2, and L_3 represent the bridge sites between B-B, B-C, and C = C bonds, respectively, and H_1 and H_2 are the hollow sites of the hexagonal and octagonal rings, respectively. To account for the interaction between adjacent adsorbed atoms, we constructed a $3\times2\times1$ supercell for the adsorption of a single Li/Na atom. The optimization results showed that when Li/Na adsorbs at C_1, B_1, or L_2, it spontaneously moves to the H_1 site, while adsorption at C_2 or L_3 leads to movement to the H_2 site. The adsorption energy can be accurately calculated using the following Eq. (4):

$$E_{ads} = E_{Li/Na+k-B_2C_3} - E_{k-B_2C_3} - E_{Li/Na} \tag{4}$$

In the equation, $E_{Li/Na+k-B_2C_3}$ represents the adsorption energy, $E_{k-B_2C_3}$ and $E_{Li/Na}$ refer to the energies of the system before and after the adsorption of Li/Na atoms, respectively, while $E_{Li/Na}$ represents the energy of a single Li/Na atom. A negative value of adsorption energy indicates that the adsorption process is spontaneous, and the more negative the value, the greater the released energy and the more stable the system after adsorption[38].

As shown in Fig. 4b, the adsorption energies of Li and Na atoms at the eight possible adsorption sites are presented. The lowest adsorption energies for both Li and Na occur at the H_1 site, with adsorption energies of −0.873 eV and −0.753 eV, respectively. Therefore, H_1 is the most stable adsorption site.

To gain deeper insights into the interaction mechanism of k-B_2C_3 with Li and Na atoms, we calculated the charge density difference for a single atom adsorbed at the H_1 site using Eq. (5):

$$\Delta\rho = \rho_{Li/Na+k-B_2C_3} - \rho_{k-B_2C_3} - \rho_{Li/Na} \tag{5}$$

In the equation, $\Delta\rho$ represents the charge density difference, $\rho_{Li/Na+k-B_2C_3}$ and $\rho_{k-B_2C_3}$ refer to the charge densities of the system before and after the adsorption of the Li/Na atom, respectively, and $\rho_{Li/Na}$ represents the charge density of a single Li/Na atom. The calculation results are shown in Fig. 5, where the yellow region represents electron transfer to the surface, and the cyan region represents electron transfer from the surface. It is clearly observed that electrons transfer from the Li/Na atom to the k-B_2C_3 surface. Bader analysis further indicates that at the H_1 site, Li and Na atoms transfer 0.89 |e| and 0.86 |e|, respectively, to the k-B_2C_3 surface. Since Li has a smaller radius and higher reactivity compared to Na, Li is more readily adsorbed closer to the k-B_2C_3 surface[39], as shown in Fig. 5c, d. The electron transfer between the Li/Na atoms and the k-B_2C_3 surface is indicative of chemisorption, where the formation of chemical bonds is driven by the electron redistribution.

The diffusion rate of Li/Na ions directly influences the charge and discharge rates of batteries. To explore this, we considered two potential diffusion pathways from H_1 to adjacent H_1 positions in the k-B_2C_3 structure (Fig. 6a, Path 1 and Path 2). Based on these pathways, the diffusion barriers for Li and Na ions were calculated using the CI-NEB method, with the results shown in Fig. 6b. Along Path 2, two barrier peaks are observed, as Li/Na ions need to traverse two C-B bonds to reach the equivalent position. In contrast, along Path 1, only one B-B bond needs to be crossed. The lowest diffusion barriers for Li and Na ions are 0.55 eV and 0.17 eV, corresponding to Path 2 and Path 1, respectively. Therefore, Li ions are more likely to diffuse along Path 2, while Na ions preferentially diffuse along Path 1. For Li ion diffusion, Path 2 has a lower diffusion barrier than Path 1, due to the more stable H_2 position along Path 2, with a diffusion barrier of 0.55 eV, which is superior to typical 2D materials such as phosphorene (0.76 eV)[40], borophene (0.60 eV)[41], and silicon (0.57 eV)[33]. In contrast to Li ion diffusion, Na ions, due to the higher stability of the B1 position, more readily diffuse along Path 1, with a diffusion barrier of 0.17 eV, which is lower than the diffusion barrier of B_2C_3 (0.23 eV)[22]. These results demonstrate that k-B_2C_3 exhibits excellent diffusion capabilities, which can enhance the charge and discharge rates of battery materials.

Theoretical capacity and open-circuit voltage of Li/Na on k-B_2C_3

As the core component of lithium/sodium-ion batteries, the performance of the anode material is not only influenced by the adsorption and diffusion of Li/Na ions but also by the Li ion storage capacity and the average

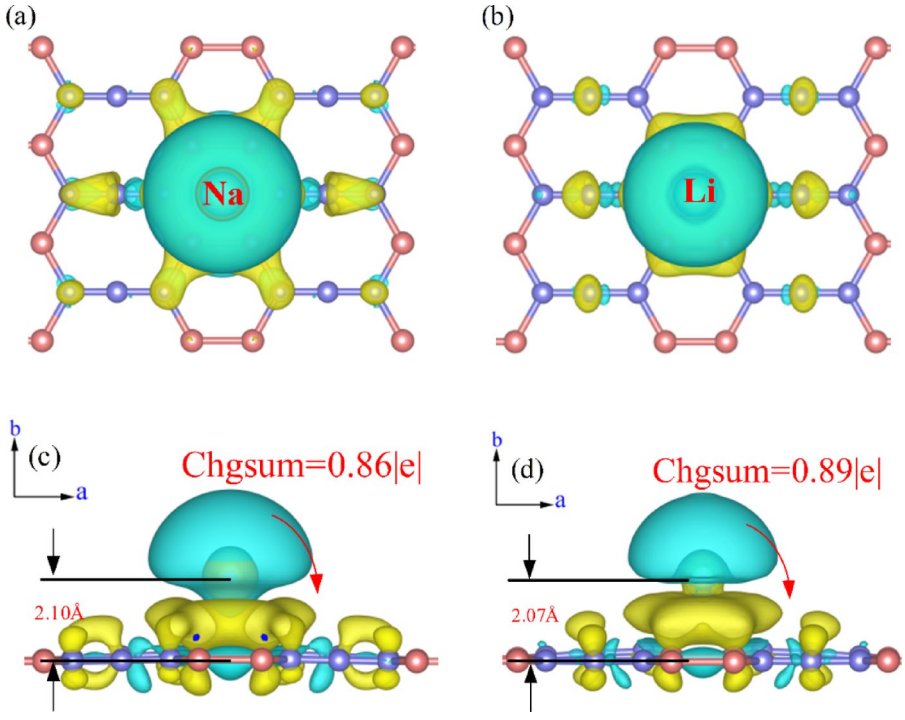

Fig. 5. (**a**) and (**b**) Top views of the differential charge density distribution for a single Li and Na atom adsorbed at the H_1 site on k-B_2C_3, respectively, highlighting the electron transfer from the Li/Na atom t the k-B_2C_3 surface. (**c**) and (**d**) Side views corresponding to (**a**) and (**b**), showing the electron redistribution across the surface.

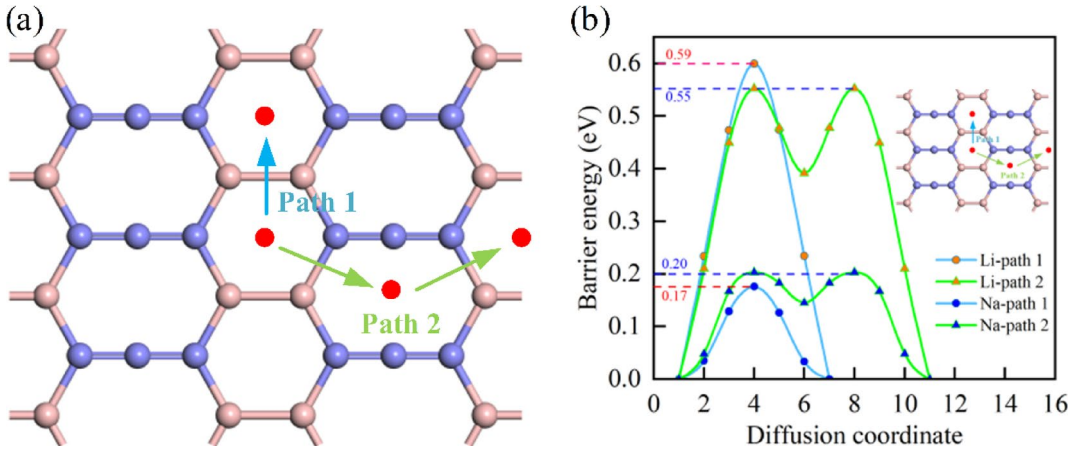

Fig. 6. Li/Na ion diffusion behavior on the *k*-B_2C_3 monolayer. (**a**) Diffusion paths of Li/Na ions (Path 1 and Path 2). (**b**) Corresponding energy barriers for Li and Na ions along the diffusion paths.

insertion potential, both of which are critical indicators of battery performance. A low and stable insertion potential helps ensure a high output voltage, while a higher specific capacity improves the battery's energy density. To investigate the theoretical specific capacity and average open-circuit voltage, we used a 3 × 2 × 1 k-B_2C_3 monolayer as the substrate. Li/Na atoms were randomly placed on both sides of the *k*-B_2C_3 monolayer, and all possible atomic configurations were optimized. The adsorption configurations were further optimized to determine the most stable adsorption sites, continuing until the maximum adsorption capacity and the most stable structure were achieved This resulted in a series of configurations with stoichiometries of Mn *k*-B_2C_3 (M = Li, Na, n = 1/3, 2/3, 1, 4/3, 5/3, 2). By calculating the average energy of Li/Na adsorption on the *k*-B_2C_3 monolayer, we obtained the maximum possible adsorption number. The average adsorption energy (E_{ads}) is calculated using the following formula (6):

$$E_{ads} = \frac{E_{M_n(k-B_2C_3)} - E_{k-B_2C_3} - nE_M}{n} \tag{6}$$

The total energy $E_{M_n(k-B_2C_3)}$ corresponds to the energy of the *k*-B_2C_3 monolayer with *n* lithium/sodium atoms adsorbed on both sides, while $E_{k-B_2C_3}$ represents the energy of the bare *k*-B_2C_3 monolayer and E_{M_n} is the energy of a single metal (Li/Na) atom. According to our definition, a negative adsorption energy indicates an exothermic adsorption process[42]. The structures and average adsorption energies for the E_{ads} configurations are shown in Fig. 7a, b. For both Li and Na, we found that the average adsorption energies were negative when *n* = 1/3, 2/3, 1, 4/3, 5/3, and 2, indicating stable intermediate phases for the $M_{n(k-B_2C_3)}$ configurations (M = Li, Na, and n = 1/3, 2/3, 1, 4/3, 5/3, 2), with a maximum of 12 Li/Na atoms adsorbed.

To further investigate the stability of Li_2 *k*-B_2C_3 and Na_2 *k*-B_2C_3, we performed a 3 ps AIMD simulation at 300 K. The structures of all Li_2 *k*-B_2C_3 and Na_2 *k*-B_2C_3 configurations remained stable during the simulation, as shown in Fig. 7c, d. The energy variation trends were relatively stable, indicating that the materials possess good thermodynamic stability.

The theoretical specific capacity (C) for the maximum adsorption configuration of M_n *k*-B_2C_3 can be evaluated using the following formula (7):

$$C = \frac{qnF}{M_{k-B_2C_3}} \tag{7}$$

where q represents the charge number of Li/Na adsorbed on each unit of the *k*-B_2C_3 monolayer, and n represents the number of Li or Na atoms adsorbed on each unit of the *k*-B_2C_3 monolayer. *F* is Faraday's constant (26,801 mAh mol^{-1}), and $M_{k-B_2C_3}$ is the molar mass of *k*-B_2C_3. The calculated maximum theoretical capacities of *k*-B_2C_3 for Li and Na are 930 $mAhg^{-1}$. As shown in Fig. 8, the energy storage capacity of *k*-B_2C_3 is compared with several other 2D anode materials[43–46]. The maximum capacity of *k*-B_2C_3 is lower than that of B_2C (1596/1596 $mAhg^{-1}$)[22,47], β_{12}-borophene (1984/1984 $mAhg^{-1}$)[48], and *k*-C_6B_4 (1395/1395 $mAhg^{-1}$)[49], but higher than most other anode materials[50–52].

The formula for calculating the average open-circuit voltage (OCV) is as follows (8):

$$OCV = \frac{-E_{M_{n_2}(k-B_2C_3)} + E_{M_{n_1}(k-B_2C_3)} + (n_2 - n_1)\,E_M}{(n_2 - n_1)\,e} \tag{8}$$

where $E_{M_{n_2}(k-B_2C_3)}$ and $E_{M_{n_1}(k-B_2C_3)}$ represent the total energies of the *k*-B_2C_3 monolayer with n_2 and n_1 Li/Na atoms adsorbed, respectively. E_M is the energy of a single atom in bulk metallic lithium or sodium. As shown in Fig. 9, the open-circuit voltage (OCV) decreases with the increasing number of adsorbed Li/Na

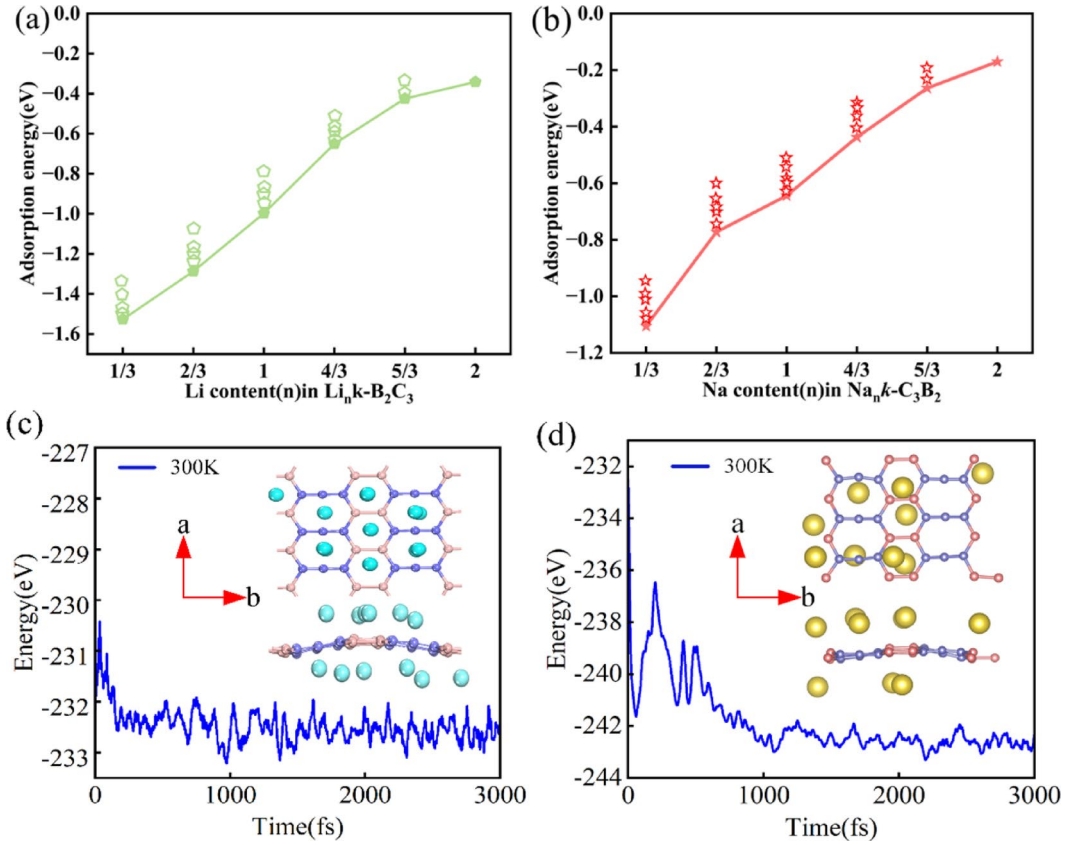

Fig. 7. (**a**) and (**b**) Show the adsorption energies of $M_n k$-B_2C_3 (M = Li, Na) at different concentrations. The triangles and pentagons represent the positions of Li and Na atoms, respectively, which were randomly and uniformly placed, centered at H_1. (**c**) and (**d**) Display the AIMD simulations for the 3 × 2 × 1 supercell of the k-B_2C_3 monolayer with 12 atoms adsorbed, illustrating the stability of the system.

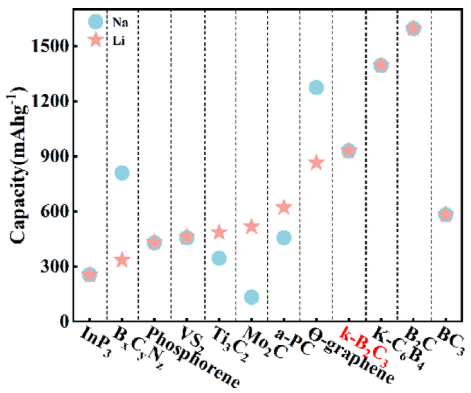

Fig. 8. Maximum LIB/NIB capacity of k-B_2C_3 monolayer compared to other 2D anode materials.

atoms. The average OCV of Li decreases from 1.297 V to 0.542 V, and the average OCV of Na decreases from 1.174 V to 0.341 V. These low voltage values are comparable to those of other materials, such as B_2C (Li average voltage = 0.57 V, Na average voltage = 0.43 V), β_{12}-borophene (Li: 0.89–0.53 V, Na: 0.60–0.27 V), and k-C_6B_4 (Li: 0.86–0.59 V, Na: 0.76–0.34 V). The relatively low average voltage values of k-B_2C_3 indicate its potential to effectively prevent the formation of Li/Na dendrites, thus ensuring the high safety and stability of Lithium/Sodium-ion batteries, making it a promising candidate as a potential electrode material for Li/Na batteries.

Conclusions

In this study, we investigated the electrochemical properties and performance of k-B_2C_3 as a potential electrode material for lithium and sodium-ion batteries. Our results show that k-B_2C_3 exhibits excellent stability and

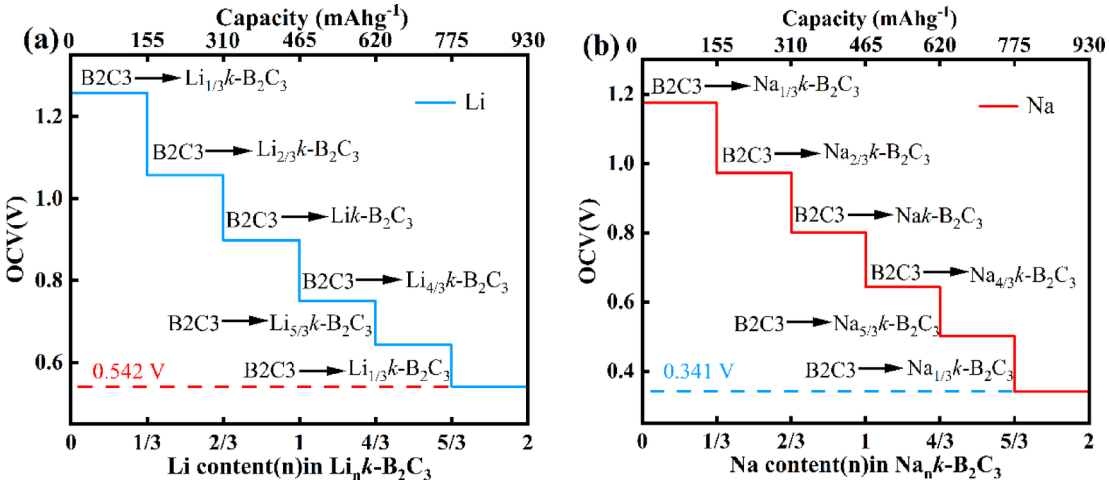

Fig. 9. (**a**) The average voltage and specific capacity of the k-B_2C_3 monolayer at different concentrations of Li. (**b**) The average voltage and specific capacity of the k-B_2C_3 monolayer at different concentrations of Na.

conductivity for both Li and Na ions. The diffusion barriers calculated for Li and Na ions along different paths demonstrate that k-B_2C_3 offers efficient ion diffusion. Specifically, the diffusion energy barriers for Li and Na ions were found to be 0.55 eV and 0.17 eV, respectively, with Li favoring path 2 and Na preferring path 1. These low barriers indicate that k-B_2C_3 could effectively facilitate fast charging and discharging processes in batteries. The maximum theoretical capacity of k-B_2C_3 was calculated to be 930 $mAhg^{-1}$ for both Li and Na ions, which is competitive with other 2D materials, although slightly lower than materials such as B_2C and β_{12}-borophene. Furthermore, the average open-circuit voltage (OCV) of k-B_2C_3 was calculated to be 1.297 V for Li and 1.174 V for Na, showing a decreasing trend with increasing ion concentration. These voltage values are comparable to other materials, such as B_2C and β_{12}-borophene, indicating that k-B_2C_3 could offer stable energy output over multiple cycles. The study also highlights that k-B_2C_3 prevents dendrite formation, enhancing the safety and stability of Li/Na batteries. Overall, k-B_2C_3 demonstrates promising potential as a high-performance electrode material for future energy storage systems.

Data availability

The datasets used and/or analysed during the current study available from the corresponding author on reasonable request.

Received: 8 January 2025; Accepted: 30 April 2025
Published online: 07 May 2025

References

1. Lu, X. et al. Polymer-based solid-state electrolytes for high-energy-density Lithium-ion batteries: Review. *Adv. Energy Mater.* **13**(38), 2301746 (2023).
2. Xu, J. et al. High-energy Lithium-ion batteries: recent progress and a promising future in applications. *Energy Environ Mater* **6**(5), e12450 (2023).
3. Assat, G. & Tarascon, J. M. Fundamental understanding and practical challenges of anionic redox activity in Li-ion batteries. *Nat. Energy* **3**(5), 373–386 (2018).
4. Acebedo, B. et al. Current status and future perspective on lithium metal anode production methods. *Adv. Energy Mater.* **13**(13), 2203744 (2023).
5. Li, C. et al. Low in-plane atomic density phosphorene anodes for lithium-/sodium-ion batteries. *J. Mater. Chem. C* **9**(21), 6802–6814 (2021).
6. Wu, J. et al. MoSe2 nanosheets embedded in nitrogen/phosphorus co-doped carbon/graphene composite anodes for ultrafast sodium storage. *J. Power Sources* **476**, 228660 (2020).
7. He, M., Zhang, L. & Li, J. Theoretical investigation on interactions between lithium ions and two-dimensional halide perovskite for solar-rechargeable batteries. *Appl. Surf. Sci.* **541**, 148509 (2021).
8. Yang, C. et al. Is graphite nanomesh a promising anode for the Na/K-Ions batteries?. *Carbon* **176**, 242–252 (2021).
9. Abu, S. M. et al. State of the art of lithium-ion battery material potentials: An analytical evaluations, issues and future research directions. *J. Clean. Prod.* **394**, 136246 (2023).
10. Kang, D. et al. Spontaneous cross-linking for fabrication of nanohybrids embedded with size-controllable particles. *ACS Nano* **10**(1), 889–898 (2016).
11. Lin, H. et al. Semi-metallic PC5 monolayer as a superior anode material for potassium ion batteries: A first principles study. *Colloids Surf. A* **643**, 128756 (2022).
12. Sun, B. et al. Micron-sized encapsulated-type MoS2/C hybrid particulates with an effective confinement effect for improving the cycling performance of LIB anodes. *J. Mater. Chem. A* **6**(15), 6289–6298 (2018).
13. Lian, R. et al. Q-carbon: a new carbon allotrope with a low degree of s–p orbital hybridization and its nucleation lithiation process in Lithium-ion batteries. *ACS Appl. Mater. Interfaces.* **12**(1), 619–626 (2020).
14. Riyanto, E. et al. Lithium-ion battery performance improvement using two-dimensional materials. *Mater. Today: Proc.* **87**, 164–171 (2023).

15. Vincent, T., Liang, J., Singh, S., *et al*. Opportunities in electrically tunable 2D materials beyond graphene: Recent progress and future outlook. *Appl. Phys. Rev.* 2021, **8**(4).
16. Liu, X. et al. Nanostructured metal oxides and sulfides for Lithium-Sulfur batteries. *Adv. Mater.* **29**(20), 1601759 (2017).
17. Ladha, D. G. A review on density functional theory–based study on two-dimensional materials used in batteries. *Mater. Today Chem.* **11**, 94–111 (2019).
18. Li, X., Wang, Q. & Jena, P. ψ-Graphene: A new metallic allotrope of planar carbon with potential applications as anode materials for lithium-ion batteries. *J. Phys. Chem. Lett.* **8**(14), 3234–3241 (2017).
19. Zhang, W., Lu, J. & Guo, Z. Challenges and future perspectives on sodium and potassium ion batteries for grid-scale energy storage. *Mater. Today* **50**, 400–417 (2021).
20. Cheng, D. L., Yang, L. C. & Zhu, M. High-performance anode materials for Na-ion batteries. *Rare Met.* **37**(3), 167–180 (2018).
21. Zhang, W. et al. Two-dimensional phosphorus carbide as a promising anode material for lithium-ion batteries. *J. Mater. Chem. A* **6**(25), 12029–12037 (2018).
22. Yu, X. et al. Metallic B2C monolayer as a promising anode material for Li/Na ion storage. *Chem. Eng. J.* **406**, 126812 (2021).
23. Yu, T. et al. Stable and metallic two-dimensional TaC2 as an anode material for lithium-ion battery. *J. Mater. Chem. A* **5**(35), 18698–18706 (2017).
24. Hafner, J. Ab-initio simulations of materials using VASP: Density-functional theory and beyond. *J. Comput. Chem.* **29**(13), 2044–2078 (2008).
25. Kresse, G. & Joubert, D. From ultrasoft pseudopotentials to the projector augmented-wave method. *Phys. Rev. B* **59**(3), 1758–1775 (1999).
26. Perdew, J. P., Burke, K. & Ernzerhof, M. Generalized gradient approximation made simple. *Phys. Rev. Lett.* **77**(18), 3865–3868 (1996).
27. Woollam, J. A. & Somoano, R. B. Superconducting critical fields of alkali and alkaline-earth intercalates of MoS2. *Phys. Rev. B* **13**(9), 3843–3853 (1976).
28. Henkelman, G., Uberuaga, B. P. & Jónsson, H. A climbing image nudged elastic band method for finding saddle points and minimum energy paths. *J. Chem. Phys.* **113**(22), 9901–9904 (2000).
29. Baroni, S. et al. Phonons and related crystal properties from density-functional perturbation theory. *Rev. Mod. Phys.* **73**(2), 515–562 (2001).
30. Rosales-Pelaez, P. et al. Seeding approach to nucleation in the N V T ensemble: The case of bubble cavitation in overstretched Lennard Jones fluids. *Phys. Rev. E* **101**(2), 022611 (2020).
31. Heyd, J., Scuseria, G. E. & Ernzerhof, M. Hybrid functionals based on a screened coulomb potential. *J. Chem. Phys.* **118**(18), 8207–8215 (2003).
32. Xiao, B. et al. Penta-graphene: A promising anode material as the Li/Na-Ion battery with both extremely high theoretical capacity and fast charge/discharge rate. *ACS Appl. Mater. Interfaces* **8**(51), 35342–35352 (2016).
33. Wang, H. et al. Siligraphene as a promising anode material for lithium-ion batteries predicted from first-principles calculations. *Nano Energy* **49**, 67–76 (2018).
34. Cheng, Z. et al. Pentagonal B2C monolayer with extremely high theoretical capacity for Li-/Na-ion batteries. *Phys. Chem. Chem. Phys.* **23**(10), 6278–6285 (2021).
35. Wang, B. et al. Ultrathin semiconducting Bi2Te2S and Bi2Te2Se with high electron mobilities. *J. Phys. Chem. Lett.* **9**(3), 487–490 (2018).
36. Yu, S. et al. Elastic properties of the solid electrolyte Li7La 3Zr2O12(LLZO). *Chem. Mater.* **28**(1), 197–206 (2016).
37. Mortazavi, B. et al. Boron–graphdiyne: A superstretchable semiconductor with low thermal conductivity and ultrahigh capacity for Li, Na and Ca ion storage. *J. Mater. Chem. A* **6**(23), 11022–11036 (2018).
38. Ferguson, D., Searles, D. J. & Hankel, M. Biphenylene and phagraphene as Lithium-ion battery anode materials. *ACS Appl. Mater. Interfaces.* **9**(24), 20577–20584 (2017).
39. Cheng, Y. et al. Three dimensional metallic carbon from distorting sp3-bond. *Cryst. Growth Des.* **16**(3), 1360–1365 (2016).
40. Xiao, X. et al. The potential application of black and blue phosphorene as cathode materials in rechargeable aluminum batteries: A first-principles study. *Phys. Chem. Chem. Phys.* **21**(13), 7021–7028 (2019).
41. Zhang, X. et al. Borophene as an extremely high capacity electrode material for Li-ion and Na-ion batteries. *Nanoscale* **8**(33), 15340–15347 (2016).
42. Ferguson, D., Searles, D. J. & Hankel, M. Biphenylene and phagraphene as Lithium ion battery anode materials. *ACS Appl. Mater. Interfaces.* **9**(24), 20577–20584 (2017).
43. Jiang, H. et al. Ab initio prediction and characterization of phosphorene-like SiS and SiSe as anode materials for sodium-ion batteries. *Sci. Bull.* **62**(8), 572–578 (2017).
44. Er, D. et al. Ti3C2 MXene as a high capacity electrode material for metal (Li, Na, K, Ca) ion batteries. *ACS Appl. Mater. Interfaces.* **6**(14), 11173–11179 (2014).
45. Wang, W. et al. First-principles investigations of vanadium disulfide for lithium and sodium ion battery applications. *RSC Adv.* **6**(60), 54874–54879 (2016).
46. Deng, S. et al. Two-dimensional MnO2 as a better cathode material for lithium ion batteries. *J. Phys. Chem. C* **119**(52), 28783–28788 (2015).
47. Reddy, B. V. & Khanna, S. N. Metallocarbohedrenes: A new class of metal-carbon assemblies. *J. Phys. Chem.* **98**(38), 9446–9449 (1994).
48. Grixti, S., Mukherjee, S. & Singh, C. V. Two-dimensional boron as an impressive lithium-sulphur battery cathode material. *Energy Storage Mater.* **13**, 80–87 (2018).
49. Kong, D. et al. Novel two-dimensional C6B4 monolayer as an anode for Li-/Na-ion batteries with high theoretical capacity. *Appl. Surf. Sci.* **616**, 156468 (2023).
50. Banerjee, S., Neihsial, S. & Pati, S. K. First-principles design of a borocarbonitride-based anode for superior performance in Sodium-ion batteries and capacitors. *J. Mater. Chem. A* **4**(15), 5517–5527 (2016).
51. Sun, Q. et al. Ab initio prediction and characterization of Mo2C monolayer as anodes for lithium-ion and sodium-ion batteries. *J. Phys. Chem. Lett.* **7**(6), 937–943 (2016).
52. Belasfar, K. et al. First-principles study of BC3 monolayer as anodes for lithium-ion and sodium-ion batteries applications. *J. Phys. Chem. Solids* **139**, 109319 (2020).

Acknowledgements

The authors gratefully acknowledge financial support from the National Natural Science Foundation of China (Grant No.51301144).

Author contributions

X.Z. and K. W. contributed equally to this work and should be considered co-first authors. X. Z.: Conceptualization, Methodology, Software. K. W.: Writing—Original Draft, Software, Validation Data curation. B. M.: Software, Validation Data curation. X. W.: Software, Validation. Writing—Review. D. K.: Writing—Review &

Editing: Y. W.: Supervision, Project administration.All authors reviewed the manuscript.

Declarations

Competing interests
The authors declare no competing interests.

Additional information
Supplementary Information The online version contains supplementary material available at https://doi.org/10.1038/s41598-025-00754-4.

Correspondence and requests for materials should be addressed to D.K. or Y.W.

Reprints and permissions information is available at www.nature.com/reprints.

Publisher's note Springer Nature remains neutral with regard to jurisdictional claims in published maps and institutional affiliations.

Open Access This article is licensed under a Creative Commons Attribution-NonCommercial-NoDerivatives 4.0 International License, which permits any non-commercial use, sharing, distribution and reproduction in any medium or format, as long as you give appropriate credit to the original author(s) and the source, provide a link to the Creative Commons licence, and indicate if you modified the licensed material. You do not have permission under this licence to share adapted material derived from this article or parts of it. The images or other third party material in this article are included in the article's Creative Commons licence, unless indicated otherwise in a credit line to the material. If material is not included in the article's Creative Commons licence and your intended use is not permitted by statutory regulation or exceeds the permitted use, you will need to obtain permission directly from the copyright holder. To view a copy of this licence, visit http://creativecommons.org/licenses/by-nc-nd/4.0/.

© The Author(s) 2025